JOURNAL OF PROPULSION AND POWER
Vol. 25, No. 4, July–August 2009

Rotational Flowfields in Porous Channels with Arbitrary Headwall Injection

Tony Saad* and Joseph Majdalani†
University of Tennessee Space Institute, Tullahoma, Tennessee 37388

DOI: 10.2514/1.41926

In this paper, Taylor's incompressible and rotational flow in a porous channel with surface mass addition is extended to account for arbitrary headwall injection. Our analysis considers Euler's steady-state equations from which an approximate solution is derived. The resulting mean flow representation satisfies the vanishing axial velocity condition at the blowing walls and is confirmed through comparisons with inviscid finite volume numerical simulations. For a given class of symmetric headwall injection profiles, our solutions are exact at the sidewall and along the midsection plane, where the error in the approximations vanishes identically. The case of uniform injection stands as an exception due to its discontinuity at the sidewall. All solutions become increasingly more accurate in the downstream direction. They hence enable us to approximate the bulk flowfield in both hybrid and solid rockets with variable headwall injection.

I. Introduction

TAYLOR'S simple analytical solution for the mean gaseous motion in solid rocket motors (SRMs) was obtained under the assumptions of steady, incompressible, rotational, and axisymmetric conditions [1]. Despite its strictly inviscid origin, its streamlines observed the vanishing axial velocity requirement at the porous sidewalls, where a blown-off boundary layer is established [2]. In recent work, Majdalani and Saad [3] presented a closed-form inviscid solution for the axisymmetric Taylor–Culick flow with arbitrary headwall injection; their model was suitable for describing the bulk fluid motion in a porous cylinder with surface mass addition. In this paper, we investigate the two-dimensional porous channel and explore additional solutions and headwall injection conditions. Obtaining an analytical model for the planar problem not only adds to our repertoire of approximations for mean flowfields, but also carries the advantage of providing an avenue for comparison with experimental and numerical studies of slit flows and slab burner grains in both hybrid and solid rocket systems. These configurations are becoming increasingly more popular in reactive flow investigations and in technological applications involving flow through porous media, starting with the original Taylor profile itself [1]. Examples abound as a host of research studies have been conducted in two-dimensional settings. To cite a few, one may enumerate, in reverse chronological order: Fischbach et al. [4]; Féraille and Casalis [5]; Fabignon et al. [6]; Chu et al. [7]; Najjar et al. [8]; Griffond [9]; Apte and Yang [10,11]; Griffond and Casalis [12,13]; Venugopal et al. [14,15]; Ugurtas [16]; Couton et al. [17]; Lupoglazoff and Vuillot [18]; Balakrishnan et al. [19]; Ma et al. [20,21]; Watson et al. [22]; and finally, perhaps one of the most influential in its category, is the 1986 paper by Traineau et al. [23]. The geometric and physical parameters used in Traineau's experimental and theoretical work are later adopted by several researchers such as Balakrishnan et al. [19], Venugopal et al. [14,15], and Apte and Yang [10,11]. Traineau's analysis is also used as a baseline for the compressible flow study conducted by Maicke and Majdalani [24].

Overall, our solution is intended to offer a basic cold-flow model for both solid and hybrid slab rockets. Because the porous channel flow has been shown to provide a reliable approximation for the core flowfield in a slab rocket, it can be employed in a multitude of studies seeking to examine 1) internal rocket gas dynamics, 2) flow instability, 3) particle-mean flow interactions, and 4) fluid–structure interactions. Other technological applications of two-dimensional flows with sidewall mass addition include 1) surface transpiration, 2) film cooling, 3) filtration, and 4) isotope separation. For the solid rocket motor, the headwall-to-sidewall injection-velocity ratio is typically of order unity; however, it proves to be one-to-two orders of magnitude larger for hybrids. With typical values at around 50 and above, the relatively large headwall injection ratio associated with hybrid rocket faceplates leads to the onset of a distinct stream-tube motion that permeates a vast portion of the chamber volume. To model the resulting outer field, our analysis is carried out under incompressible, inviscid, and nonreactive conditions.

The paper is organized as follows. The mathematical model is first defined along with its appropriate boundary conditions. Subsequently, a general solution for an arbitrary headwall injection profile is developed. This is followed by special applications corresponding to uniform, Berman's half-cosine, Poiseuille's, and turbulent injection profiles. Finally, a numerical comparison with inviscid flow simulations is presented, and the error in the approximations is quantified. A family of solutions that represent complex symmetric flowfields is then obtained as functional perturbations about either Berman's or Poiseuille's injection patterns.

II. Mathematical Model

The slab motor can be idealized as a two-dimensional channel of porous length L_0 and height $2a$ with both a permeable headwall and a nozzleless aft end (see Fig. 1). At the headwall, a fluid stream (which may denote an oxidizer or gaseous propellant mixture) is injected into the chamber at a maximum centerline speed U_c. This incoming stream is assimilated with the lateral crossflow, driven by uniform mass addition at the porous sidewalls. Naturally, the sidewall injection velocity U_w is commensurate with the solid-propellant or fuel regression rates. In hybrids, U_w can be appreciably smaller than U_c due to slow fuel pyrolysis, whereas these two values are the same in SRM analysis. As shown in Fig. 1, $\bar{x}$ and $\bar{y}$ stand for the axial and transverse coordinates used to describe the position from the headwall to the typical nozzle attachment point at the aft boundary. In the event that the fuel or solid-propellant burning rates are not uniform, the sidewall injection velocity may be estimated from the average value:

Presented as Paper 4120 at the 37th AIAA Fluid Dynamics Conference and Exhibit, Miami, FL, 25–28 June 2007; received 30 October 2008; revision received 9 February 2009; accepted for publication 4 March 2009.

*Doctoral Research Assistant. Member AIAA.

†H. H. Arnold Chair of Excellence in Advanced Propulsion, Mechanical, Aerospace and Biomedical Engineering Department; maji@utsi.edu. Member AIAA (Corresponding Author).

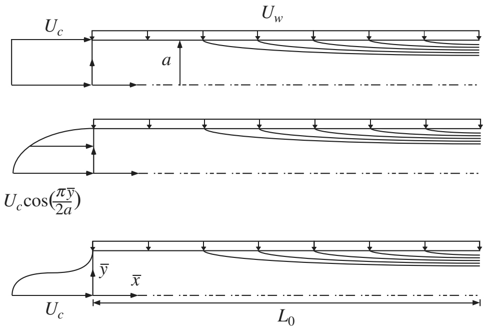

Fig. 1 Rocket chamber simulated as a porous channel with arbitrary headwall injection.

$$U_w = -\frac{1}{L_0}\int_0^{L_0} \bar{v}(\bar{x}, a)\mathrm{d}\bar{x} \tag{1}$$

A. Normalization

We begin by normalizing the principal variables and operators. This can be done by setting

$$x = \frac{\bar{x}}{a}; \qquad y = \frac{\bar{y}}{a}; \qquad \nabla = a\bar{\nabla}; \qquad p = \frac{\bar{p}}{\rho U_w^2} \tag{2}$$

$$u = \frac{\bar{u}}{U_w}; \qquad v = \frac{\bar{v}}{U_w}; \qquad \boldsymbol{\Omega} = \frac{\bar{\boldsymbol{\Omega}} a}{U_w}$$

$$\psi = \frac{\bar{\psi}}{aU_w}; \qquad u_c = \frac{U_c}{U_w}; \qquad L = \frac{L_0}{a} \tag{3}$$

Here, $U_c = \bar{u}(0,0)$ and $U_w = -\bar{v}(\bar{x}, a) = \bar{v}(\bar{x}, -a)$ allude to the centerline and uniform fluid injection velocities along the headwall and sidewalls, respectively. For steady inviscid motion, the vorticity transport equation reduces to

$$\nabla \times \boldsymbol{u} \times \boldsymbol{\Omega} = 0; \qquad \boldsymbol{\Omega} = \nabla \times \boldsymbol{u} \tag{4}$$

Assuming symmetry, we consider only half of the channel and make use of the standard stream function. This enables us to write the following.

For no flow across the midsection plane,

$$v(x, 0) = -\psi_x(x, 0) = 0 \tag{5a}$$

For vanishing axial velocity at the sidewall,

$$u(x, 1) = \psi_y(x, 1) = 0 \tag{5b}$$

For constant sidewall mass addition,

$$v(x, 1) = -\psi_x(x, 1) = -1 \tag{5c}$$

For the headwall injection profile,

$$u(0, y) = \psi_y(0, y) = u_0(y) \tag{5d}$$

where

$$u = \psi_y; \qquad v = -\psi_x \tag{6}$$

B. Vorticity-Stream-Function Formulation

Recognizing that the vorticity has a single nonzero spanwise component (in the z direction), one can turn Eq. (4) into

$$\nabla^2\psi = -\Omega \tag{7}$$

As usual, the next step is to substitute into the vorticity transport equation given by Eq. (4). Its fulfillment beckons a functional relation for Ω of the form

$$\Omega = F(\psi) \quad \text{since} \quad \frac{(\Omega)_x}{(\Omega)_y} = \frac{[F(\psi)]_x}{[F(\psi)]_y} = \frac{F_\psi \psi_x}{F_\psi \psi_y} = \frac{\psi_x}{\psi_y} \tag{8}$$

A useful choice can be shown to be

$$\Omega = C^2\psi \tag{9}$$

Despite the nonuniqueness of this relation, it leads to a model that permits the assimilation of the four boundary conditions in Eq. (5). In fact, straightforward substitution into Eq. (7) yields the Helmholtz equation:

$$\nabla^2\psi + C^2\psi = 0 \tag{10}$$

III. Solution

Using separation of variables, the solution of Eq. (10) is found to be

$$\psi(x, y) = (\alpha x + \beta)[A\cos(Cy) + B\sin(Cy)] \tag{11}$$

We note that, by linearity, any combination of equations akin to Eq. (11) is also a solution to Eq. (10). Implementation of the four constraints may be systematically carried out, preferably in the order in which they appear. For instance, Eq. (5a) gives

$$\psi_x(x, 0) = \alpha A\cos(Cy) + \alpha B\sin(Cy)|_{y=0} = 0 \tag{12}$$

This implies that $A = 0$. With no loss in generality, we set $B = 1$ and rewrite Eq. (5b) as

$$\psi_y(x, 1) = C(\alpha x + \beta)\cos(C) = 0 \quad \text{or} \quad C_n = (n + \tfrac{1}{2})\pi \quad \forall\ n \in \{0, 1, 2, 3, \ldots, \infty\} \tag{13}$$

The ensuing eigenfunctions take the form

$$\psi_n = (\alpha_n x + \beta_n)\sin[(n + \tfrac{1}{2})\pi y] \tag{14}$$

Using $C_n = (n + \frac{1}{2})\pi$ enables us to sum over eigenfunctions that alternate between wall suction and injection. The total solution can be obtained via superposition. We collect

$$\psi(x, y) = \sum_{n=0}^{\infty}(\alpha_n x + \beta_n)\sin\left[\left(n + \frac{1}{2}\right)\pi y\right] \tag{15}$$

A. Taylor-Type Solutions

At this juncture, we can resume implementing the problem's constraints. Forthwith, the auxiliary condition given by Eq. (5c) yields

$$\psi_x(x, 1) = \sum_{n=0}^{\infty}\alpha_n \sin\left[\left(n + \frac{1}{2}\right)\pi\right] = 1 \quad \text{or} \quad \sum_{n=0}^{\infty}(-1)^n\alpha_n = 1 \tag{16}$$

Several distinct solutions may therefore exist depending on the choice of $\{\alpha_n\}$. Here, we shall focus on the case leading to Taylor's; this may be uniquely recovered by setting

$$\alpha_0 = 1 \quad \text{and} \quad \alpha_n = 0 \quad \forall\ n \neq 0 \tag{17}$$

Lastly, the headwall boundary condition renders

$$\psi_y(0, y) = \frac{1}{2}\pi\sum_{n=0}^{\infty}(2n + 1)\beta_n \cos\left[\left(n + \frac{1}{2}\right)\pi y\right] = u_0(y) \tag{18}$$

Orthogonality may then be imposed to retrieve $\{\beta_n\}$; one recovers

$$\beta_n \int_0^1 (2n + 1)\cos^2\left[\left(n + \frac{1}{2}\right)\pi y\right]\mathrm{d}y = (2/\pi)\int_0^1 u_0(y)\cos\left[\left(n + \frac{1}{2}\right)\pi y\right]\mathrm{d}y \tag{19}$$

or

$$\beta_n = \frac{4}{(2n + 1)\pi}\int_0^1 u_0(y)\cos\left[\left(n + \frac{1}{2}\right)\pi y\right]\mathrm{d}y \tag{20}$$

The extended Taylor solution is thus at hand. Based on Eq. (15), one can put

Table 1 Stream function, axial velocity, and vorticity for several headwall injection patterns[a]

u_0	0 (inert)	u_c	$u_c\cos(\frac{1}{2}\pi y)$	$u_c(1-y^2)$	$u_c(1-y)^8$
ψ	$x\sin\zeta$	$x\sin\zeta + 8u_c\sum_{n=0}^{\infty}\frac{(-1)^n}{d_n^2}\sin\eta$	$(x+u_h)\sin\zeta$	$x\sin\zeta + 64u_c\sum_{n=0}^{\infty}\frac{(-1)^n}{d_n^4}\sin\eta$	$x\sin\zeta + u_c\sum_{n=0}^{\infty}\frac{(-1)^n}{d_n^{10}}\sigma\sin\eta$
u	$\frac{1}{2}\pi x\cos\zeta$	$\frac{1}{2}\pi x\cos\zeta + 4u_c\sum_{n=0}^{\infty}\frac{(-1)^n}{d_n}\cos\eta$	$\frac{1}{2}\pi(x+u_h)\cos\zeta$	$\frac{1}{2}\pi x\cos\zeta + 32u_c\sum_{n=0}^{\infty}\frac{(-1)^n}{d_n^3}\cos\eta$	$\frac{1}{2}\pi x\cos\zeta + \frac{1}{2}u_c\sum_{n=0}^{\infty}\frac{(-1)^n}{d_n^9}\sigma\cos\eta$
Ω	$\frac{1}{4}\pi^2 x\sin\zeta$	$\frac{1}{4}\pi^2 x\sin\zeta$	$\frac{1}{4}\pi^2(x+u_h)\sin\zeta$	$\frac{1}{4}\pi^2 x\sin\zeta + 16u_c\sum_{n=0}^{\infty}\frac{(-1)^n}{d_n^2}\sin\eta$	$\frac{1}{4}\pi^2 x\sin\zeta + \frac{1}{4}u_c\sum_{n=0}^{\infty}\frac{(-1)^n}{d_n^8}\sigma\sin\eta$

[a] Here, $d_n = (2n+1)\pi$, $\zeta = \frac{1}{2}\pi y$, $\eta = (n+\frac{1}{2})\pi y$, $u_h = (2/\pi)u_c$, and $\sigma = 1792(d_n^6 - 120d_n^4 + 5760d_n^2 - 46,080)$.

$$\psi(x,y) = x\sin\left(\frac{1}{2}\pi y\right) + \sum_{n=0}^{\infty}\beta_n\sin\left[\left(n+\frac{1}{2}\right)\pi y\right] \tag{21}$$

where

$$\beta_n = \begin{cases} 8(-1)^n u_c/[\pi^2(2n+1)^2] & u_0 = u_c \\ 2u_c/\pi;\quad n=0\quad (0\quad \forall\ n\neq 0) & u_0 = u_c\cos(\frac{1}{2}\pi y) \\ 64(-1)^n u_c/[\pi^4(2n+1)^4] & u_0 = u_c(1-y^2) \\ \{1792(-1)^n u_c/[\pi^{10}(2n+1)^{10}]\}\begin{bmatrix} -46,080 + 5760\pi^2(2n+1)^2 \\ -120\pi^4(2n+1)^4 + \pi^6(2n+1)^6 \end{bmatrix} & u_0 = u_c(1-y^8) \end{cases} \tag{22}$$

Corresponding axial and normal velocities emerge as

$$u(x,y) = \frac{1}{2}\pi x\cos\left(\frac{1}{2}\pi y\right) + \frac{1}{2}\pi\sum_{n=0}^{\infty}(2n+1)\beta_n\cos\left[\left(n+\frac{1}{2}\right)\pi y\right]$$
$$v(x,y) = -\sin\left(\frac{1}{2}\pi y\right) \tag{23}$$

Similarly, the vorticity takes the form

$$\Omega(x,y) = \frac{1}{4}\pi^2 x\sin\left(\frac{1}{2}\pi y\right) + \frac{1}{4}\pi^2\sum_{n=0}^{\infty}(2n+1)^2\beta_n\sin\left[\left(n+\frac{1}{2}\right)\pi y\right] \tag{24}$$

Based on Eq. (20), specific solutions may be secured for various inlet profiles. Here, we consider those corresponding to inert headwall (i.e., no injection), uniform injection, Berman's half-cosine, Poiseuille's, and an eighth-power polynomial to mimic turbulent flow. These are posted in Table 1. For a simulated hybrid rocket, the centerline velocities of arbitrary profiles can be calculated to produce the same flux at $x = 0$ as that due to uniform injection. A simple mass balance yields

$$\int_{-1}^{1} u_0(y)\mathrm{d}y = \int_{-1}^{1} u_c\mathrm{d}y = 2u_c \tag{25}$$

The equivalent centerline velocities for Berman's half-cosine, Poiseuille's, and turbulent flow profiles of the type $u_c(1-y^m)$ are found to be

$$u_c = \left[\frac{1}{2}\pi, \frac{3}{2}, \frac{2(m+1)}{(-1)^{m+1} + 2m + 1}\right] \tag{26}$$

Note that the third member in Eq. (26) can reproduce the Poiseuille case of $u_c = \frac{3}{2}$ for $m = 2$. Plots of the vorticity contours are shown for uniform (Fig. 2a), Berman's half-cosine (Fig. 2b), Poiseuille's (Fig. 2c), and power-law profiles (Fig. 2d). Interestingly, in the case of uniform injection, the effects of vorticity are restricted to a narrow region near the sidewall, as the corresponding flow is essentially irrotational. This may explain the absence of the headwall injection term u_c in the expression for mean flow vorticity in the third column of Table 1.

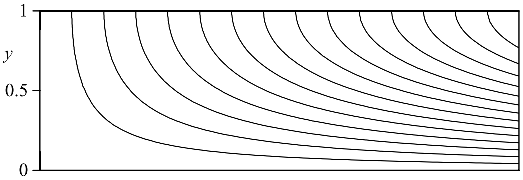

a) Uniform injection

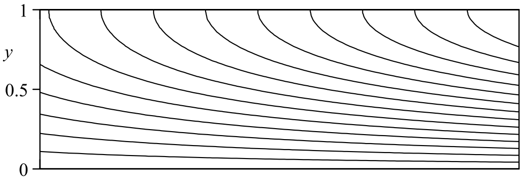

b) Berman

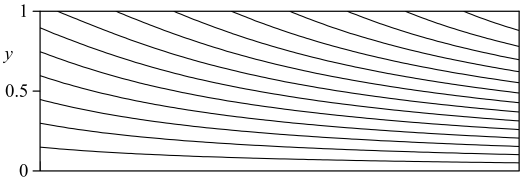

c) Poiseuille

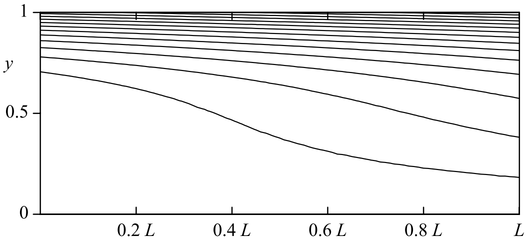

d) Power law (m = 8)

Fig. 2 Vorticity contours for a porous channel with varying headwall injection patterns and $u_c = 1$.

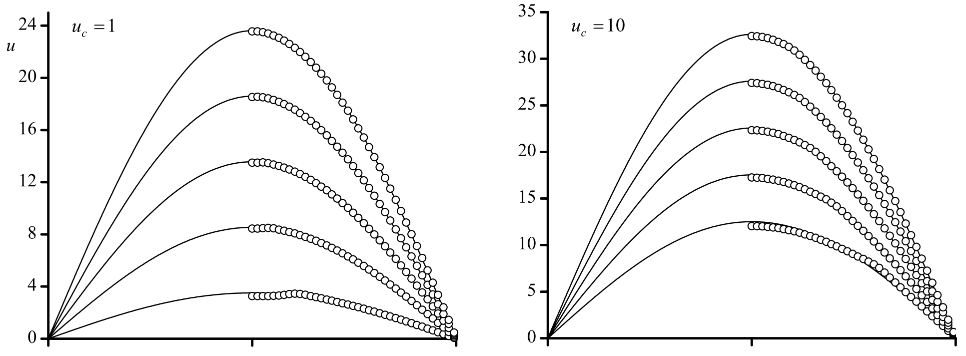

a) Berman **b) Berman**

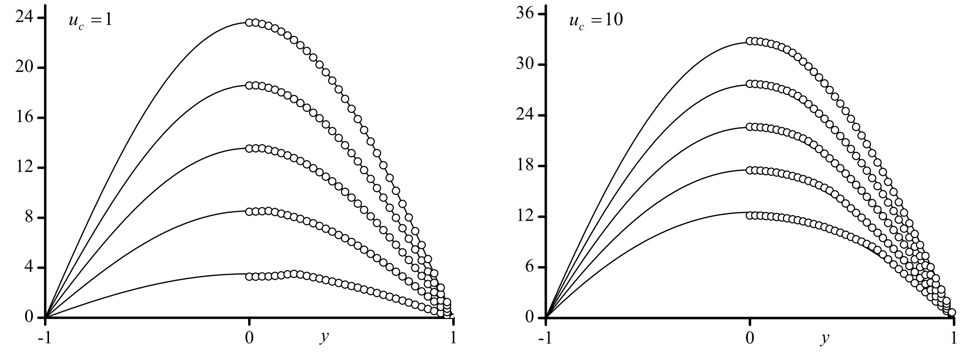

c) Poiseuille **d) Poiseuille**

Fig. 3 Comparison between analytical (lines) and numerical simulations (circles) for the axial velocities. Curves are shown for $x/L = 0.1, 0.3, 0.5, 0.7$, and 0.9.

B. Pressure Analysis

The pressure distribution can be easily obtained from $\boldsymbol{u}\cdot\nabla\boldsymbol{u} = -\nabla p$ by integrating in two spatial directions and adding the results. One obtains

$$p = k - \frac{1}{2}\boldsymbol{u}\cdot\boldsymbol{u} - \int v u_y \mathrm{d}x - \int u v_x \mathrm{d}y = k - \frac{1}{2}\boldsymbol{u}\cdot\boldsymbol{u} - \int v u_y \mathrm{d}x \qquad v \neq v(x) \tag{27}$$

where k is chosen such that $p(0,0) = p_0$. However, such integration is only possible when the integrability condition is satisfied: that is, $(p_y)_x = (p_x)_y$. This can be written in terms of the velocity field as

$$u u_{xy} + v u_{yy} = 0 \tag{28}$$

where we have used the fact that u and v satisfy the continuity equation and $v = -\sin(\frac{1}{2}\pi y)$. One finds that the constraint given by Eq. (28) is satisfied inside the chamber volume in the case of inert and half-cosine injection, whereas it is only admissible at the midsection plane for power-law profiles. For the inert and Berman profiles, one obtains

$$p(x,y) = p_0 - \tfrac{1}{8}[\pi^2 x^2 + 4u_c\pi x + 2 - 2\cos(\pi y)] \tag{29}$$

and the midsection plane pressure for the remaining injection profiles may be expressed as

$$p(x,0) = p_0 - \tfrac{1}{8}\pi x(\pi x + 4u_c) \tag{30}$$

It is interesting to note that the centerline pressure is invariant with respect to the headwall injection profile.

C. Nonlinear Residual in Vorticity Transport Equation

To test the accuracy of our solutions, we substitute Eqs. (9) and (15) into Eq. (4). Terms that do not entirely cancel are hereby referred to as the residual error $Q(x,y)$. For each eigensolution given by Eq. (14), the vorticity transport equation is satisfied and the residual error Q_n is identically zero:

$$Q_n(x,y) = (\psi_n)_x(\Omega_n)_y - (\psi_n)_y(\Omega_n)_x = C_n^2(\psi_n)_x(\psi_n)_y - C_n^2(\psi_n)_y(\psi_n)_x = 0 \tag{31}$$

where $\Omega_n = C_n^2\psi_n$ and $C_n = (n + \frac{1}{2})\pi$. Thus, when Eq. (31) is summed over all eigenmodes, it vanishes. This represents an interesting situation, albeit hypothetical, for which the eigensolutions coexist with no interaction. In practice, when coupling between the eigenmodes is entertained, the total vorticity and stream function

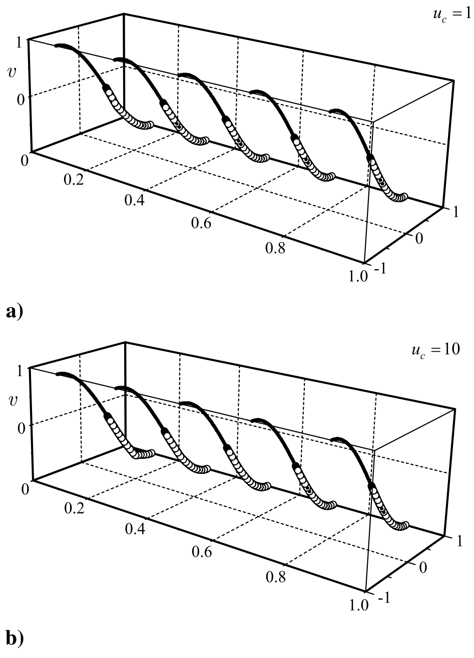

a)

b)

Fig. 4 Comparison between analytical (solid dots) and numerical simulations (hollow circles) for the transverse velocity using Berman's half-cosine injection.

given by Eq. (15) are substituted into Eq. (4). The cumulative error becomes

$$Q(x,y) = \psi_x\Omega_y - \psi_y\Omega_x = \sum_{n=0}^{\infty}(\psi_n)_x\sum_{n=0}^{\infty}(\Omega_n)_y - \sum_{n=0}^{\infty}(\psi_n)_y\sum_{n=0}^{\infty}(\Omega_n)_x \tag{32}$$

where

$$\left.\begin{array}{rr}(\psi_n)_x = \alpha_n\sin(C_n y); & (\Omega_n)_x = C_n^2(\psi_n)_x \\ (\psi_n)_y = C_n(\alpha_n x + \beta_n)\cos(C_n y); & (\Omega_n)_y = C_n^2(\psi_n)_y\end{array}\right\} \tag{33}$$

If we further take into account that for the Taylor-type solutions,

$$\alpha_0 = 1 \quad \text{and} \quad \alpha_n = 0 \quad \forall\ n \neq 0 \tag{34}$$

then Eq. (32) simplifies into

$$Q(y) = \sin(C_0 y)\sum_{n=0}^{\infty}(C_n^2 - C_0^2)(\psi_n)_y \tag{35}$$

Equation (35) represents the error in the vorticity transport equation due to nonlinear coupling of the eigenfunctions. In general, it is not zero, except in the case of self-similar headwall injection profiles such as Berman's. When $(\psi_n)_y$ is replaced by its corresponding expression given by Eq. (33), one obtains

$$Q(y) = \sin(C_0 y)\sum_{n=0}^{\infty}R_n\cos(C_n y) \tag{36}$$

where $R_n = (C_n^2 - C_0^2)C_n\beta_n$. It is clear through Eq. (36) that the residual error is controlled by R_n. This parameter embodies the deviation from the exact solution corresponding to Berman's half-cosine injection. In the case of an inert headwall, $\beta_n = R_n = 0$, and the solution is exact. As $R_n \to 0$, the solutions become more accurate. However, when $\beta_n \neq 0$, R_n will vanish when $C_n^2 = C_0^2$, as in the case of Berman's injection. To illustrate this behavior, three specific examples are given. First, for Poiseuille's injection, one gets

$$R_{n,\text{Poiseuille}} = \frac{8}{\pi}u_c(-1)^n[(2n+1)^{-1} - (2n+1)^{-3}] \tag{37}$$

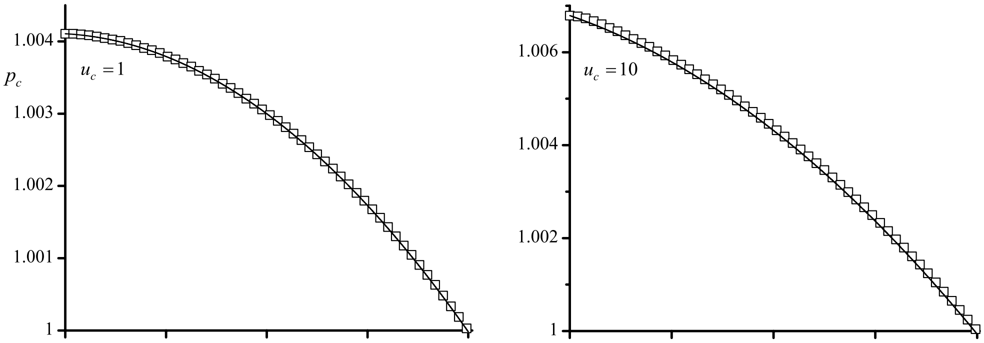

a) Berman **b) Berman**

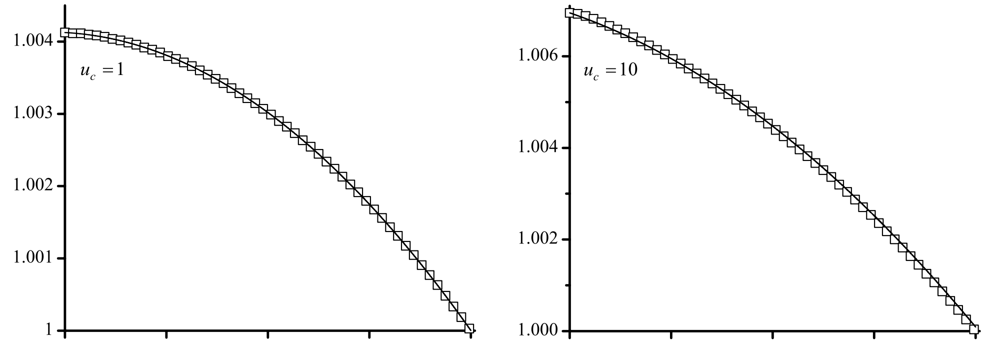

c) Poiseuille **d) Poiseuille**

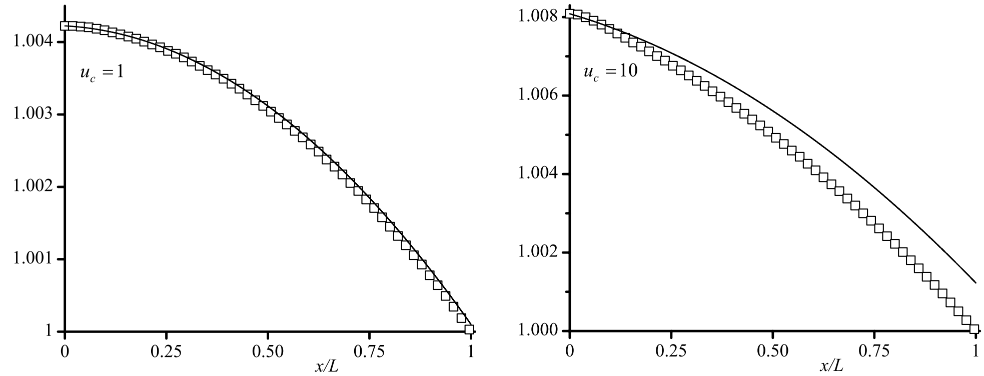

e) Power law (*m* = 8) **f) Power law (*m* = 8)**

Fig. 5 Comparison between analytical (lines) and numerical simulations (squares) for the centerline pressure.

This term quickly converges to zero with successive increases in n. In this case, the residual is sufficiently small but nonzero, because only the first few terms of Eq. (37) contribute to the residual error. Second, for the case of a power-law profile, one collects

$$R_{n,\text{power law}} = \frac{\pi^2}{4}[(2n+1)^2 - 1](-1)^n u_c d_n^{-10}\sigma \tag{38}$$

where

$$d_n = (2n+1)\pi$$

and

$$\sigma = 1792(d_n^6 - 120d_n^4 + 5760d_n^2 - 46,080)$$

Here too, although Eq. (38) converges to zero quite rapidly, the first few terms are relatively larger than their counterparts in the Poiseuille case. Third, for uniform injection, one arrives at

$$R_{n,\text{uniform}} = \pi u_c (-1)^n [(2n+1) - (2n+1)^{-1}] \tag{39}$$

This residual remains undefined because the alternating sequence of increasing terms in Eq. (39) diverges. Note that whenever Eq. (36) converges, the residual is identically zero both at the midsection plane and at the chamber sidewalls. Moreover, being independent of the axial position, the residual becomes proportionately smaller in long porous channels such as those associated with simulated rocket grains. These factors help to explain the accuracy of the present approximations for several case studies that are discussed subsequently.

D. Convergence

The absolute convergence and ratio tests can be used to show that the series obtained herein are convergent. For the sake of illustration, we present the procedure used for the case of uniform injection, being the most intransigent of the group. Starting with the stream function

$$\psi(x,y) = x\sin\left(\frac{1}{2}\pi y\right) + 8u_c \sum_{n=0}^{\infty} \frac{(-1)^n}{\pi^2(2n+1)^2}\sin\eta$$

$$\eta = \left(n + \frac{1}{2}\right)\pi y \tag{40}$$

the absolute convergence test may be applied to show that

$$\sum_{n=0}^{\infty}\left|\frac{(-1)^n}{(2n+1)^2}\sin\eta\right| \le \sum_{n=0}^{\infty}\frac{1}{(2n+1)^2} \tag{41}$$

where the right-hand side converges to $\frac{1}{8}\pi^2$. The axial velocity obtained using term-by-term differentiation returns

$$u(x,y) = \frac{1}{2}\pi x\cos\left(\frac{1}{2}\pi y\right) + 4\frac{u_c}{\pi}\sum_{n=0}^{\infty}\frac{(-1)^n}{(2n+1)}\cos\eta \tag{42}$$

The summation in Eq. (42) is the Fourier series representation of a square wave and is therefore a convergent sum. Finally, to obtain the vorticity, we make use of closed-form representations of summations to avoid the pitfalls of term-by-term differentiation. In this case, the second term in Eq. (42) may be written as the sum of two inverse tangents:

$$\sum_{n=0}^{\infty}\frac{(-1)^n}{(2n+1)}\cos\eta = \frac{1}{2}[\tan^{-1}(e^{-\frac{1}{2}i\pi y}) + \tan^{-1}(e^{\frac{1}{2}i\pi y})] \tag{43}$$

The derivative of Eq. (43) vanishes inside the channel as well as at the sidewall. The latter is obtained by taking the limit as $y \to 1$.

IV. Numerical Verification

By way of verification, we present a numerical solution for the inviscid flow equations and several headwall injection profiles. The simulations are carried out using a two-dimensional finite volume code. These are based on a chamber with an average sidewall velocity of 1 m/s and purely inviscid conditions. The aspect ratio is chosen to be $L = 16$ and the actual size of the domain is 1.6×0.1 m.

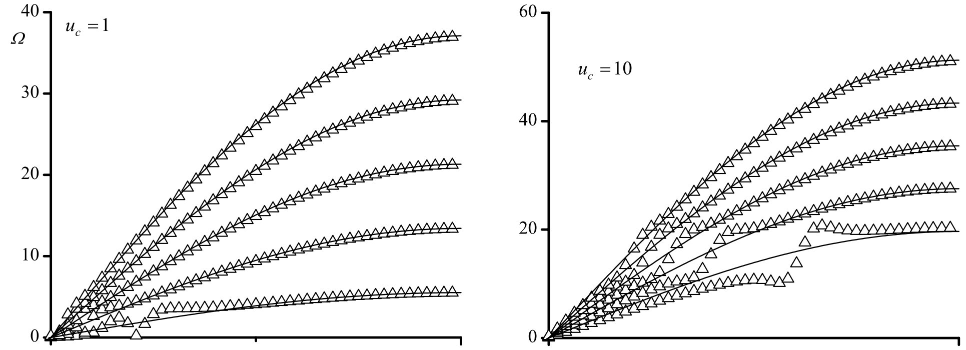

a) Berman **b) Berman**

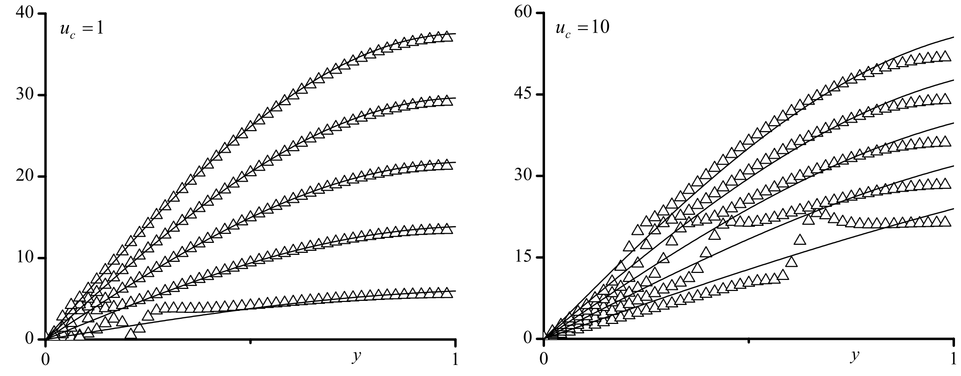

c) Poiseuille **d) Poiseuille**

Fig. 6 Comparison between analytical (lines) and numerical vorticity (triangles) with headwall injection constants of $u_c = 1$ (left) and 10 (right).

We use a fine mesh of 589,824 equally spaced control volumes numbering 3072 × 192. A first-order upwind scheme is resorted to for spatial discretization and the SIMPLE algorithm is applied to resolve pressure-velocity coupling. The boundary conditions at the sidewalls are specified as velocity inlets with $U_w = 1\ \mathrm{m/s}$ to closely mimic the mathematical model whereby injection is imposed uniformly along the grain surface. The headwall is also specified as a velocity inlet with $U_c = 1$ and $10\ \mathrm{m/s}$. On the right-hand side of the domain, a pressure outlet boundary condition is prescribed with a pressure corresponding to atmospheric conditions. Although an outflow boundary condition can also be assumed at the downstream section, it is discounted here to avoid the potential case of partially developed flow. At the midsection plane, a symmetry condition is imposed. Finally, the working fluid is taken to be air at standard conditions.

Some results of our inviscid simulations are shown in Figs. 3–6. In Figs. 3 and 4, the axial and transverse velocities are plotted for $u_c = 1$ and 10, respectively. In both figures, the streamwise evolution of the velocities is depicted in the forward segment of the chamber, in which the curves are located at $x/L = 0.1$, 0.3, 0.5, 0.7, and 0.9. These particular axial positions are consistently used to display our results in the remainder of this study. Using identical inviscid conditions in both numerical and analytical models, the agreement with the numerics is seen to gradually improve with further flow development.

In Fig. 5, the centerline pressure is plotted for $u_c = 1$ and 10. The reference pressure p_0 is obtained from the computational data at $(x, y) = (0, 0)$ and then used in Eq. (30) to generate the analytical baseline. For convenience, the pressure is normalized by the atmospheric pressure p_{atm} taken at 101,325 Pa: namely, by setting $p_c = \bar{p}_c / p_{\mathrm{atm}}$. For $u_c = 1$, the agreement is excellent for all injection profiles, and for $u_c = 10$, the best agreement is for Berman's and Poiseuille's, followed by the power-law profile.

Finally, in Fig. 6, the vorticity is displayed for $u_c = 1$ and 10. The agreement is seen to be excellent at $u_c = 1$ for both Berman and Poiseuille injections. At $u_c = 10$ the agreement continues to hold, especially when removed from the headwall. However, in the vicinity of the headwall, smoothing of the numerically obtained curves is required to improve the agreement with the analytical solutions.

Despite the comparison being limited in scope, it reaffirms the viability of the analytical approximations obtained in Sec. III. For

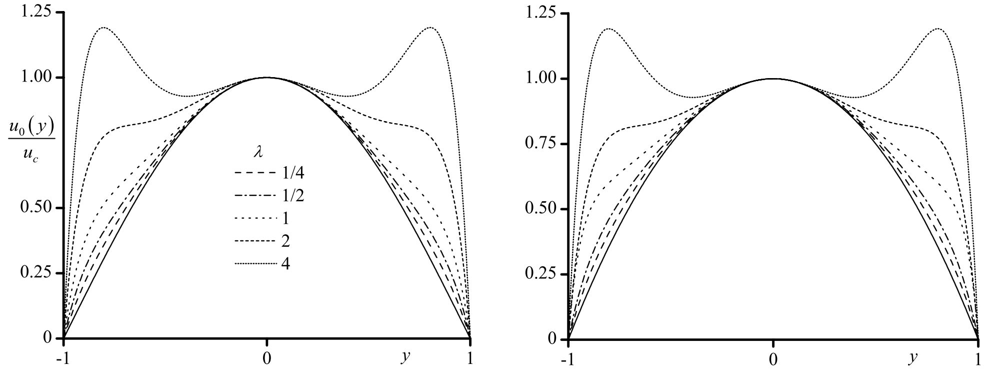

a) Berman-based polynomials

b) Poiseuille-based polynomials

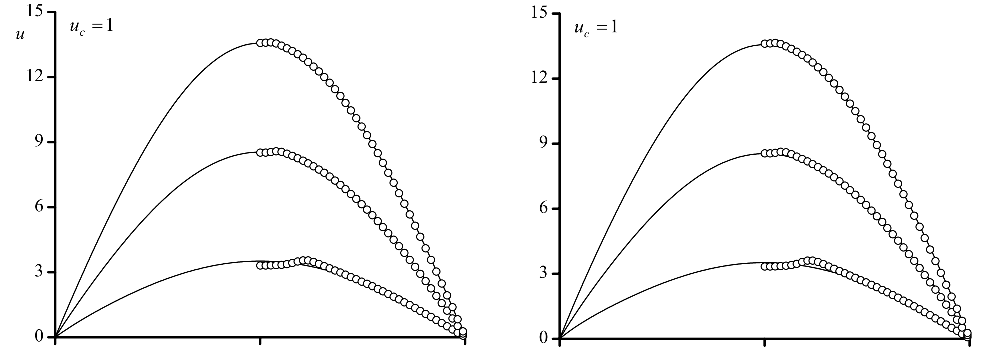

c) λ = 0.25

d) λ = 0.5

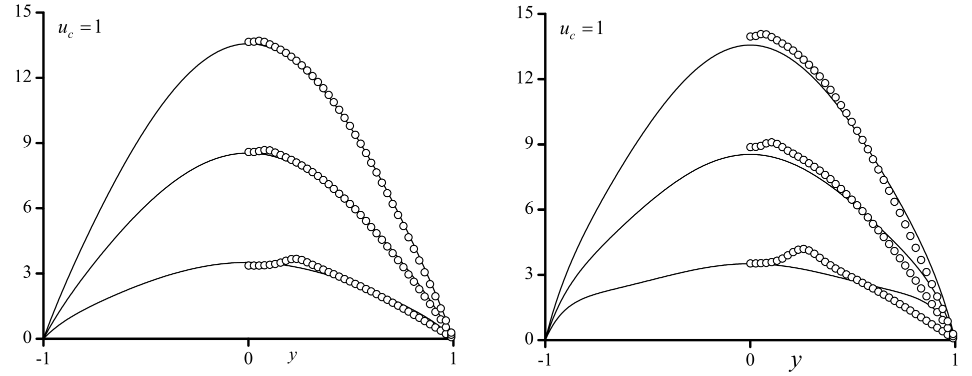

e) λ = 1

f) λ = 4

Fig. 7 Comparison between polynomial-based injection solutions (lines) and numerical simulations (circles). The comparison with numerics is shown for $x/L = 0.1$, 0.3, and 0.5.

larger values of u_c, the inviscid simulation diverges, thus necessitating the use of a turbulence model. At this point, the comparison between the analytical solution and the turbulent simulations ceases to be relevant.

V. Modeling Irregular Injection Patterns

For injection profiles that are close to Berman's half-cosine, it is clear that the present solution provides a useful approximation. If one introduces a set of profiles with a finite departure from Berman's half-cosine, the resulting solutions can then be used to approximate more complex flowfields. Given that the Poiseuille injection profile closely resembles Berman's, both may be used as a basis for generating a polynomial with the facility to reproduce complex injection patterns. This is accomplished by setting the power series:

$$\frac{u_0(y)}{u_c} = f(y) + \lambda \sum_{m=2}^{2k+1} (-y^2)^m = f(y) + \lambda(y^4 - y^6 + \cdots) \quad (44)$$

where

$$f(y) = \begin{cases} \cos(\frac{1}{2}\pi y) \\ 1 - y^2 \end{cases} \quad (45)$$

In Eq. (44), $(4k + 2)$ is the power-series order, and $\lambda \geq 0$ is a control parameter. One must take $k \leq 4$ to ensure convergence of the infinite series in Eq. (21). In practice, setting $k > 4$ leads to unphysical injection profiles. Note that the summation in Eq. (44) includes an even number of terms to allow the velocity to vanish at the sidewalls. The power-series order affects the bluntness of the profile at $y = \pm 1$ and λ controls its breadth. This behavior may be seen in Figs. 7a and 7b, in which different parametric combinations are used. Here, profiles represent functional perturbations with respect to 1) Berman's and 2) Poiseuille's injection. Numerical simulations (Figs. 7c–7f) use four terms ($k = 2$) and four values of λ, as shown. These are based on Poiseuille's parabolic profile and a headwall injection constant of $u_c = 1$. In Figs. 7c–7f, a comparison between the analytical solutions and numerical simulations is presented for this family of profiles. The agreement appears to be satisfactory for all cases considered, given that they represent functional perturbations about the exact solution. In closing, we note that regardless of the initial deviation from the cosine shape, the ensuing motion rapidly evolves into Taylor–Culick's self-similar form.

VI. Conclusions

In this study, we derive approximate solutions for the inviscid incompressible Taylor flow in a two-dimensional porous channel with arbitrary headwall injection. Our solutions closely mimic numerical simulations of this problem while securing the no-slip boundary condition at the sidewalls. This is especially true for the hybrid model, in which the large headwall injection velocity offsets the secondary crossflow effect caused by small sidewall injection at the fore-end corner points. The known singularity in the planar Taylor flow at $x = 0$ is mitigated in the hybrid representation (i.e., for large headwall-to-sidewall injection). Furthermore, provided that headwall mass addition is kept constant, the effect of varying the headwall injection shape is found to be negligible in sufficiently long chambers. Our analysis enables us to capture several headwall injection patterns, including complex flowfields defined as functional perturbations about the similarity-conforming Berman or Poiseuille injection.

Acknowledgments

This project was funded by the National Science Foundation through grant CMMI-0353518, Eduardo A. Misawa, Program Director.

References

[1] Taylor, G. I., "Fluid Flow in Regions Bounded by Porous Surfaces," *Proceedings of the Royal Society of London, Series A: Mathematical and Physical Sciences*, Vol. 234, No. 1199, 1956, pp. 456–475. doi:10.1098/rspa.1956.0050

[2] Culick, F. E. C., "Rotational Axisymmetric Mean Flow and Damping of Acoustic Waves in a Solid Propellant Rocket," *AIAA Journal*, Vol. 4, No. 8, 1966, pp. 1462–1464. doi:10.2514/3.3709

[3] Majdalani, J., and Saad, T., "The Taylor–Culick Profile with Arbitrary Headwall Injection," *Physics of Fluids*, Vol. 19, No. 9, 2007, Paper 093601. doi:10.1063/1.2746003

[4] Fischbach, S. R., Majdalani, J., and Flandro, G. A., "Acoustic Instability of the Slab Rocket Motor," *Journal of Propulsion and Power*, Vol. 23, No. 1, 2007, pp. 146–157. doi:10.2514/1.14794

[5] Féraille, T., and Casalis, G., "Channel Flow Induced by Wall Injection of Fluid and Particles," *Physics of Fluids*, Vol. 15, No. 2, 2003, pp. 348–360. doi:10.1063/1.1530158

[6] Fabignon, Y., Dupays, J., Avalon, G., Vuillot, F., Lupoglazoff, N., Casalis, G., and Prévost, M., "Instabilities and Pressure Oscillations in Solid Rocket Motors," *Journal of Aerospace Science and Technology*, Vol. 7, No. 3, 2003, pp. 191–200. doi:10.1016/S1270-9638(02)01194-X

[7] Chu, W.-W., Yang, V., and Majdalani, J., "Premixed Flame Response to Acoustic Waves in a Porous-Walled Chamber with Surface Mass Injection," *Combustion and Flame*, Vol. 133, No. 3, 2003, pp. 359–370. doi:10.1016/S0010-2180(03)00018-X

[8] Najjar, F. M., Haselbacher, A., Ferry, J. P., Wasistho, B., Balachandar, S., and Moser, R., "Large-Scale Multiphase Large-Eddy Simulation of Flows in Solid-Rocket Motors," AIAA Paper 2003-3700, June 2003.

[9] Griffond, J., "Receptivity and Aeroacoustic Resonance in Channels with Blowing Walls," *Physics of Fluids*, Vol. 14, No. 11, 2002, pp. 3946–3962. doi:10.1063/1.1511546

[10] Apte, S., and Yang, V., "Unsteady Flow Evolution in a Porous Chamber with Surface Mass Injection. Part 2: Acoustic Excitation," *AIAA Journal*, Vol. 40, No. 2, 2002, pp. 244–253. doi:10.2514/2.1666

[11] Apte, S., and Yang, V., "Unsteady Flow Evolution in a Porous Chamber with Surface Mass Injection. Part I: Free Oscillation," *AIAA Journal*, Vol. 39, No. 8, 2001, pp. 1577–1586. doi:10.2514/2.1483

[12] Griffond, J., and Casalis, G., "On the Nonparallel Stability of the Injection Induced Two-Dimensional Taylor Flow," *Physics of Fluids*, Vol. 13, No. 6, 2001, pp. 1635–1644. doi:10.1063/1.1367869

[13] Griffond, J., and Casalis, G., "On the Dependence on the Formulation of Some Nonparallel Stability Approaches Applied to the Taylor Flow," *Physics of Fluids*, Vol. 12, No. 2, 2000, pp. 466–468. doi:10.1063/1.870323

[14] Venugopal, P., Najjar, F. M., and Moser, R. D., "Numerical Simulations of Model Solid Rocket Motor Flows," AIAA Paper 2001-3950, July 2001.

[15] Venugopal, P., Najjar, F. M., and Moser, R. D., "DNS and LES Computations of Model Solid Rocket Motors," AIAA Paper 2000-3571, July 2000.

[16] Ugurtas, B., Avalon, G., Lupoglazoff, N., Vuillot, F., and Casalis, G., "Stability and Acoustic Resonance of Internal Flows Generated by Side Injection," *Solid Propellant Chemistry, Combustion, and Motor Interior Ballistics*, Vol. 185, edited by V. Yang, T. B. Brill, and W.-Z. Ren, Progress in Astronautics and Aeronautics, AIAA, Washington, D.C., 2000, pp. 823–836.

[17] Couton, D., Doan-Kim, S., and Vuillot, F., "Numerical Simulation of Vortex-Shedding Phenomenon in a Channel with Flow Induced through Porous Wall," *International Journal of Heat and Fluid Flow*, Vol. 18, No. 3, 1997, pp. 283–296. doi:10.1016/S0142-727X(97)00005-2

[18] Lupoglazoff, N., and Vuillot, F., "Numerical Simulation of Vortex Shedding Phenomenon in Two-Dimensional Test Case Solid Rocket Motors," AIAA Paper 92-0776, Jan. 1992.

[19] Balakrishnan, G., Liñan, A., and Williams, F. A., "Compressible Effects in Thin Channels with Injection," *AIAA Journal*, Vol. 29, No. 12, 1991, pp. 2149–2154. doi:10.2514/3.10852

[20] Ma, Y., Van Moorhem, W. K., and Shorthill, R. W., "Experimental Investigation of Velocity Coupling in Combustion Instability," *Journal of Propulsion and Power*, Vol. 7, No. 5, 1991, pp. 692–699. doi:10.2514/3.23381

[21] Ma, Y., Van Moorhem, W. K., and Shorthill, R. W., "Innovative Method of Investigating the Role of Turbulence in the Velocity Coupling Phenomenon," *Journal of Vibration and Acoustics*, Vol. 112, No. 4, 1990, pp. 550–555. doi:10.1115/1.2930141

[22] Watson, E. B. B., Banks, W. H. H., Zaturska, M. B., and Drazin, P. G., "On Transition to Chaos in Two-Dimensional Channel Flow Symmetrically Driven by Accelerating Walls," *Journal of Fluid Mechanics*, Vol. 212, No. 1, 1990, pp. 451–485. doi:10.1017/S0022112090002051

[23] Traineau, J. C., Hervat, P., and Kuentzmann, P., "Cold-Flow Simulation of a Two-Dimensional Nozzleless Solid-Rocket Motor," AIAA Paper 86-1447, July 1986.

[24] Maicke, B. A., and Majdalani, J., "On the Rotational Compressible Taylor Flow in Injection-Driven Porous Chambers," *Journal of Fluid Mechanics*, Vol. 603, May 2008, pp. 391–411. doi:10.1017/S0022112008001122

J. Oefelein
Associate Editor